Acta Materialia 253 (2023) 118968

Contents lists available at ScienceDirect

Acta Materialia

journal homepage: www.elsevier.com/locate/actamat

Ni-Nb-P-based bulk glass-forming alloys: Superior material properties combined in one alloy family

Lucas M. Ruschel [a,*], Oliver Gross [b], Benedikt Bochtler [b], Bosong Li [c], Bastian Adam [a], Nico Neuber [a], Maximilian Frey [a], Sergej Jakovlev [a], Fan Yang [d], Hao-Ran Jiang [a,e], Bernd Gludovatz [c], Jamie J. Kruzic [c], Ralf Busch [a]

[a] Chair of Metallic Materials, Saarland University, Saarbrücken 66123, Germany
[b] Amorphous Metal Solutions GmbH, Homburg 66424, Germany
[c] School of Mechanical and Manufacturing Engineering, University of New South Wales (UNSW Sydney), Sydney, NSW 2052, Australia
[d] Institute of Materials Physics in Space, German Aerospace Center (DLR), Köln 51147, Germany
[e] Materials Genome Institute, Shanghai University, Shanghai 200444, China

ARTICLE INFO

Keywords:
Bulk metallic glass
Ni-Nb alloys
Phosphorous
High-strength material
Glass-forming ability
Electrostatic levitation

ABSTRACT

Ni-Nb-based bulk glass-forming alloys are among the most promising amorphous metals for industrial applications due to their incomparable combination of strength, hardness, elasticity and plasticity. However, the main drawback is the limited glass-forming ability, narrowing the field of application to solely small components. In this study, we show that minor additions of P to the binary Ni-Nb system increase the glass-forming ability by 150 % to a record value of 5 mm. P can be easily added by using an industrial Ni-P pre-alloy which is readily available. The partial substitution of Nb by Ta further boosts the glass-forming ability to values 200 % higher than that of the binary base alloy. Besides conventional X-ray diffraction measurements, the amorphous nature of the samples is verified by high-energy synchrotron X-ray diffraction experiments. Moreover, the mechanical properties of the new alloy compositions are characterized in uniaxial compression tests and Vickers hardness measurements, showing a high engineering yield strength of 3 GPa, an extended plastic regime up to 10 % strain to failure and an increase of the hardness to a maximum value of 1000 HV5. Additionally, calorimetric measurements reveal that the modified alloys feature an extended supercooled liquid region up to 69 K upon heating, permitting thermoplastic micro molding of amorphous feedstock material.

1. Introduction

Metallic glasses do not exhibit grain boundaries, crystal defects or slip planes due to their disordered, amorphous structure. This results in unique physical and chemical properties such as high strength, high hardness, improved corrosion resistance and good soft magnetic properties [1,2]. On the downside, many metallic glasses can only be produced in micrometer thick dimensions, since high cooling rates are required to suppress crystallization. To address this issue, extensive research and great efforts have been made to develop new metallic glasses with high glass forming ability (GFA). These alloys are generally tailored starting from one or more deep binary eutectics, leading to a multicomponent alloy with typically three to five elements. This results in dense liquids with viscosities that are several orders of magnitude higher than in simple metallic liquids. Their high packing density and their tendency to develop short and medium range order brings them thermodynamically closer to the thermodynamic ground state. These factors suppress crystallization from the kinetic as well as thermodynamic point of view [3–5]. During this alloy development process over the past decades, many glass forming systems were developed such as Zr- [6], Ni- [7], Cu- [8], Fe- [9], Au- [10] or Pd- [11] based compositions. Systems with a critical casting thickness d_c, which defines the maximum attainable amorphous casting size, of 1 mm or greater are classified as bulk metallic glasses (BMGs). Among the mentioned classes of alloys, Ni-based metallic glasses feature high strength [12,13], an excellent corrosion resistance and an extended application field due to a very high glass transition temperature [12–15], attracting technological interest as class of engineering-oriented materials.

The binary Ni-Nb system is a promising starting point for alloy development, as it shows two deep eutectics on the Ni-rich side. Of

* Corresponding author.
E-mail address: lucas.ruschel@uni-saarland.de (L.M. Ruschel).

https://doi.org/10.1016/j.actamat.2023.118968
Received 30 January 2023; Received in revised form 6 April 2023; Accepted 28 April 2023
Available online 28 April 2023

particular interest is the eutectic $Ni_{58.5}Nb_{41.5,}$ as it stabilizes the liquid state down to low temperatures, promoting glass formation [16]. Moreover, Chathoth et al. demonstrated slow dynamics of the eutectic composition due to an exceptionally high packing fraction in the liquid state [17]. Small variations in the Ni to Nb ratio resulted in a binary BMG ($Ni_{62}Nb_{38}$) featuring a high critical casting thickness of 2 mm [18]. Such a high GFA is unusual for metallic binary systems, which can commonly only be produced in thicknesses of a few micrometers. Other systems known to solidify as BMGs in the binary state are for instance the Cu-Zr [19] or Ni-Ta system [20]. Due to the relative simplicity of the binary system coupled with high GFA, in-depth research to understand the glass formation process is of particular interest. For instance, Xia et al. analyzed the glass formation in the Ni-Nb system from a thermodynamic point of view by calculating the formation enthalpies for different compositions and predicted $Ni_{61.5}Nb_{38.5}$ as the best glass-forming alloy, which is in good agreement with the experimentally determined composition $Ni_{62}Nb_{38}$ [18]. Vijay et al. [21] and Xu et al. [22] performed molecular dynamics studies based on Voronoi cluster analysis and attributed the improved GFA around a Nb content of 38 at% to a drastic increase in the population of icosahedral-like clusters during cooling from the liquid to the glassy state. For metallic glass systems in general, a pronounced icosahedral short-range order is anticipated with a slowdown of the melt dynamics, resulting in improved GFA [23–25]. Further enhancement in the Ni-Nb system required the introduction of additional elements such as Sn, Zr, Ta, and Ti. By adding Sn, the critical casting thickness was improved to 3 mm and the width of the supercooled liquid region (SCLR) upon heating was increased to 58 K [26]. Similar results were obtained for injection molding by adding Zr or Ta as a third element. However, the GFA never exceeded the threshold of 3 mm in these ternary systems [12,27]. Further additions of elements to obtain quaternary compositions have only led to marginal effects, as in the case of $Ni_{57}Nb_{33}Zr_5Co_5$, where the GFA was increased to 3.5 mm [12]. To date, no significant breakthrough in improving the GFA was achieved, restricting the widespread use of this high strength material in structural engineering applications [12,26-28].

A successful approach in alloy development of BMGs is so-called minor alloying, also referred to as micro-alloying, where metallic glasses with improved properties and enhanced GFA were produced if the proper minor alloying addition is chosen for the respective base alloy. Especially metalloids such as Si [29], S [8] or B [26] are of particular interest as micro-alloying elements due to their highly negative enthalpy of mixing and small atomic diameter with respect to the other constituent elements, contributing to the three Inoue criteria for glass formation [30]. However, the underlying mechanism facilitating glass formation at metalloid contents of 1–2 at% is not yet fully understood, whereas the degradation at higher contents is often connected to the formation of crystalline compounds with high melting temperature [31]. Phosphorus is another prominent alloying element in BMGs and is present in some of the best-known glass-forming systems such as Pd-Ni-P [32], Pt-P [33], Fe-P [34] and Ni-P [35]-based bulk glass forming alloys. Yet, it is usually alloyed in quantities above 10 at% and not used as a micro-alloying element, which is primarily related to the presence of deep eutectics in many binary metal-phosphorous systems. However, the production of alloys with such a high P content is challenging and expensive, restricting their industrial relevance. Kawashima et al. investigated lower amounts of P (5 at%) in the Ni-Nb system regarding their corrosion properties but did not observe any improvement in GFA compared to the binary $Ni_{62}Nb_{38}$ alloy [18,36].

This work focuses primarily on the addition of minor amounts of P in the range of a few atomic percentages (1–4 at%) and its effects on GFA, thermal stability, solidus and liquidus temperatures, probed by calorimetry and X-ray diffraction techniques. Especially for the micro alloying technique, it is known that the maximum in GFA is usually narrow and small differences around the optimum minor-alloying content results in a sharp drop in GFA [8]. The primary precipitating phase, playing a crucial role for glass formation, is determined by container-less electrostatic levitation (ESL) in-situ high energy synchrotron diffraction experiments (HEXRD). Furthermore, HEXRD experiments are performed to investigate the amorphous structure of the newly developed alloys with the highest GFA. For a first comprehensive characterization, these are also investigated in terms of their mechanical properties using Vickers hardness and uniaxial compression testing.

2. Experimental procedure

2.1. Sample production

The master alloys were synthesized from the raw elements Ni (99.95 wt%), Nb (99.9 wt%), Ta (99.95 wt%) and P (99.999 wt%). P was added to the master alloy in form of a previously custom-made $Ni_{75}P_{25}$ (at%) pre-alloy. For this purpose, pure Ni was inductively alloyed with red P in a quartz tube under high purity argon atmosphere. As red P undergoes a phase transition from the solid state directly to the gaseous state upon heating under normal pressure, the mass of the pre-alloy was subsequently checked to detect any mass loss compared to the initial weight. The conservation of mass allows an exact determination of the composition assuming that only P is lost during the production process. The detailed production process of a similar pre-alloy is described in Refs. [37,38]. Furthermore, an industrial grade pre-alloy with the composition $Ni_{66.6}P_{33.4}$ (at%) was additionally used, which is produced and sold by the company KBM Affilips. Details on the chemical analysis of the industrial pre-alloy can be found in the supplementary information (SI). The proper amount of the pre-alloy was subsequently alloyed together with the raw elements in an electric arc furnace in a Ti-gettered argon atmosphere. The ingots were flipped and remelted at least five times to ensure a homogeneous distribution of the elements. In the next step, the critical casting thicknesses of the novel compositions were determined by casting the master alloys in water cooled copper molds using a custom-built suction casting machine. Cylindrical rods were cast in the case of the better glass formers exceeding a critical casting diameter of 2 mm, while plate-shaped specimens with varying thicknesses (0.25 mm and 0.75 mm) were produced for the poorer glass formers. The specimens for the mechanical tests were produced by the company Amorphous Metal Solutions GmbH (AMS) in Germany [39]. AMS uses a die casting method which was especially developed for casting amorphous metals in steel mold and is well-suited for the processing of these high-melting temperature alloys [40]. Different alloy development strategies were applied and the characterization of most of the developed compositions is provided in the SI (Fig. SI1, SI2 and Table SI1). This work focuses on the development along a linear connection between the two eutectics $Ni_{58.5}Nb_{41.5}$ and $Ni_{69}P_{31}$ in the ternary phase diagram (more details in the SI and Fig. SI3), since deep eutectics commonly facilitate glass formation [41]. Small amounts of P were scanned along this line and are further referred to as ‘eutectic line’ compositions. However, it should be mentioned that this is not the actual eutectic line, but only a first order approximation in form of a linear connection of the two eutectics.

2.2. Structural characterization by X-ray diffraction

X-ray diffraction (XRD) patterns of as-cast samples were recorded at room temperature on a D8-A25-Advance and PANalytical X’Pert Pro-diffractometer in Bragg-Brentano θ-θ-geometry with Cu Kα-radiation (λ=1.5406 Å). The experiments were carried out in a 2θ range of 20° to 80° with a step size of 0.013° and a total scan time of 1 h 20 min. The cross sections of the rod-shaped specimens were characterized to obtain information from the inner region of the specimen, which is most susceptible to crystal formation as it experiences the lowest cooling rate. The poorer glass formers with a critical casting size below 2 mm were fabricated in the shape of plates (the detailed mold geometry is shown in Ref. [42]) and sanded to half of their initial casting thickness with an

accuracy of ±50 μm, as this is the region experiencing the lowest cooling rate. Furthermore, HEXRD experiments were conducted in transmission geometry at the P21.2 beamline facility of PETRA III of the German Electron Synchrotron (DESY). The diffraction patterns of the bulk glass forming compositions with the highest GFA were recorded at room temperature with a VAREX XRD4343CT detector (2880×2880 pixels) using a beam energy of 70 keV (λ=0.177138 Å).

In the same beamline facility, crystallization from the equilibrium liquid was studied on levitating droplets using the same VAREX detector, but a beam energy of 97 keV (λ=0.127819 Å). Specimens weighing about 100 mg were levitated under high vacuum in an electrostatic field and heated above the liquidus temperature using a high-power infrared laser (λ=808 nm). After superheating by about 100 K, the droplets were cooled freely (cooling rate: ~20 K s^{-1}) by switching off the laser. Simultaneously, the diffraction patterns were recorded at an acquisition time of 1 s for each diffraction pattern until the end of crystallization. The temperature was recorded using a pyrometer, which was calibrated using the melting point upon heating. For detailed information on the ESL setup, the reader is referred to Ref. [43–45]. The two-dimensional diffraction patterns were integrated using PyFAI [46] and subsequently baseline-corrected with the PDFgetX2 software [47] to obtain the scattering intensity.

2.3. Scanning electron microscopy

The microstructure was investigated in a Zeiss Sigma VP scanning electron microscope (SEM) in back-scattered electron (BSE) imaging mode and the chemical composition was analyzed using an Oxford Instruments energy dispersive X-ray spectrometer (EDX).

2.4. Calorimetric measurements

Thermal analyses were performed at heating rates of 0.333 K s^{-1} under a constant high-purity argon flow (Ar. 6.0) using a Netzsch STA 449 F3 Jupiter with a TG-DSC sensor to determine the onset of the glass transition temperature T_g, the onset of the primary crystallization T_x of amorphous samples, as well as the solidus and liquidus temperatures T_m and T_l, respectively. Graphite crucibles custom coated with Y_2O_3 were used, allowing multiple melting without reactions between melt and crucible.

2.5. Mechanical testing

Uniaxial compression testing was performed for samples with compositions in the binary ($Ni_{62}Nb_{38}$), ternary ($Ni_{59.2}Nb_{38.8}P_2$) and quaternary ($Ni_{59.2}Nb_{33.8}Ta_5P_2$) Ni-Nb system. Rectangular samples with nominal dimensions of 1×1×2 mm^3 (length L x width w x height h) were cut from beam samples with dimensions of 15×1×2 mm^3. For statistical reasons, 5–6 repeat tests were conducted for each group, which amorphous structure was previously verified by XRD. The surfaces of the tungsten carbide loading platens were lubricated with molybdenum disulfide-based lubricant to minimize friction. The compression tests were conducted on ground flat and parallel samples with a displacement rate of 0.16 μm s^{-1}, using a deflection gage to measure the displacement directly on the compression platen to calculate the strain.

In addition, Vickers hardness measurements were performed using a Wolpert Wilson 930 N universal hardness tester applying a load of 49.03 N (HV5).

3. Results

3.1. Ni-Nb-P system – critical casting size, primary crystalline phases and calorimetry

Various sizes (plate-shaped: d_c<2 mm, rod-shaped: d_c≥2 mm) of the 'eutectic line' compositions, including $Ni_{58.5}Nb_{41.5}$, $Ni_{58.8}Nb_{40.2}P_1$, $Ni_{59}Nb_{39.5}P_{1.5}$, $Ni_{59.2}Nb_{38.8}P_2$, $Ni_{59.3}Nb_{38.2}P_{2.5}$, $Ni_{59.5}Nb_{37.5}P_3$, $Ni_{59.7}Nb_{36.8}P_{3.5}$ and $Ni_{59.9}Nb_{36.1}P_4$ (hereafter, P_x, where x=0, 1, 1.5, 2, 2.5, 3, 3.5, 4), were cast and analyzed by XRD to determine the critical casting thickness d_c, as shown in Fig. 1a. All diffractograms reveal a diffuse diffraction maximum, typical for monolithic metallic glasses. Casting above the critical casting size (for plates: d_c+0.5 mm, for rods: d_c+1 mm) results in partially crystalline solidification, as revealed by the appearance of many Bragg-peaks in Fig. 1b. This culminates in the maximum achievable casting thickness of up to 5 mm for P_2, surpassing binary $Ni_{62}Nb_{38}$ (d_c=2 mm [18]) by 150 %. Even at a thickness of 6 mm, a mostly amorphous pattern is evident, superimposed by the first occurrence of Bragg peaks (indicated by black arrows). This highlights that proper additions of P significantly enhance the GFA of Ni-Nb alloys, until contents above 2 at% result in a continuous decline back to 0.25 mm for P_4 comparable to the composition without P.

The primary crystalline phases were assigned based on the X-ray patterns of 4 mm as-cast samples of P_0, P_1, P_2, P_3 and P_4, as shown in Fig. 1c as well as HEXRD experiments (more details below in Fig. 2). For the Ni-Nb-based alloys P_0 and P_1, Ni_3Nb and Ni_6Nb_7 were indicated by means of the Bragg diffraction peaks, whereas higher amounts of P (P_3 and P_4) lead to the precipitation of Nb_3Ni_2P. The GFA maximum is located exactly in between, at P_2, showing a fully amorphous XRD pattern. Compositional fine adjustments around the 5 mm amorphous alloy P_2 were performed and led in both cases, higher Ni or Nb content, to a deterioration of the GFA, as can be seen in Fig. 1d from the appearance of small Bragg peaks. In addition to the high-purity Ni-P pre-alloy produced in-house, commercially available industrial-grade Ni-P was used as well. The use of industrial grade purity is accompanied by a GFA loss of 1 mm, however, an excellent d_c of 4 mm can still be achieved (circular shaped line in Fig. 1d). This simplifies the production process of Ni-Nb-P alloys, allowing industrial upscaling due to the availability of a suitable pre-alloy. More particularly, the handling of pure P can be avoided, which is generally preferable due to its volatile nature.

In order to understand the influence of P on crystallization as one important aspect of glass formation, it is essential to know their crystallization sequence, especially the primary crystalline species. One possibility to obtain insights into the crystallization from the equilibrium liquid are calorimetric cooling experiments followed by ex-situ XRD investigations in combination with microstructural analyses. However, the primary precipitating phase, which ultimately limits the GFA, cannot be determined accurately and unambiguously by this method. Therefore, container-less ESL in-situ synchrotron HEXRD experiments were performed to study the crystallization sequence upon free cooling from the equilibrium liquid of Ni-Nb alloys with and without P, specifically $Ni_{62}Nb_{38}$ and $(Ni_{62}Nb_{38})_{95}P_5$. The latter belongs to one compositional line within the ternary phase diagram investigated in this work (see Fig. SI1) and resulted from a systematic pre-study to understand the loss of the GFA due to excessive alloying of P. Both crystallization sequences are shown in the left panel of Fig. 2a and b. In both subfigures, the temperatures of the diffraction data were marked with the same color coding (red: high T, blue: low T) in the temperature cooling profile in the right panel. In the case of binary $Ni_{62}Nb_{38}$, a liquid amorphous structure is present in the range from 1648 K (above T_l) up to an undercooling of about 116 K below T_l, until primary crystallization of orthorhombic Ni_3Nb sets in at 1460 K along with the recalescence. As a result of the released heat, the subsequent phase crystallizes at higher temperatures of 1474 K and can be assigned to trigonal Ni_6Nb_7 in accordance with the binary Ni-Nb phase diagram [16]. The crystallization sequence changes due to P-addition, as can be seen for $(Ni_{62}Nb_{38})_{95}P_5$ in Fig. 2b. In addition to the phases Ni_3Nb and Ni_6Nb_7, a P-rich phase is simultaneously forming to Ni_3Nb, as indicated by the emerging Bragg peaks at a temperature of 1431 K. This is not surprising, as an alteration of the primary precipitating phase is frequently observed by micro-alloying of metalloids [31]. Based on the diffraction pattern, this additional phase could be assigned to the tetragonal intermetallic Nb_3Ni_2P, a Nb-rich phase with high P content in relation to the overall

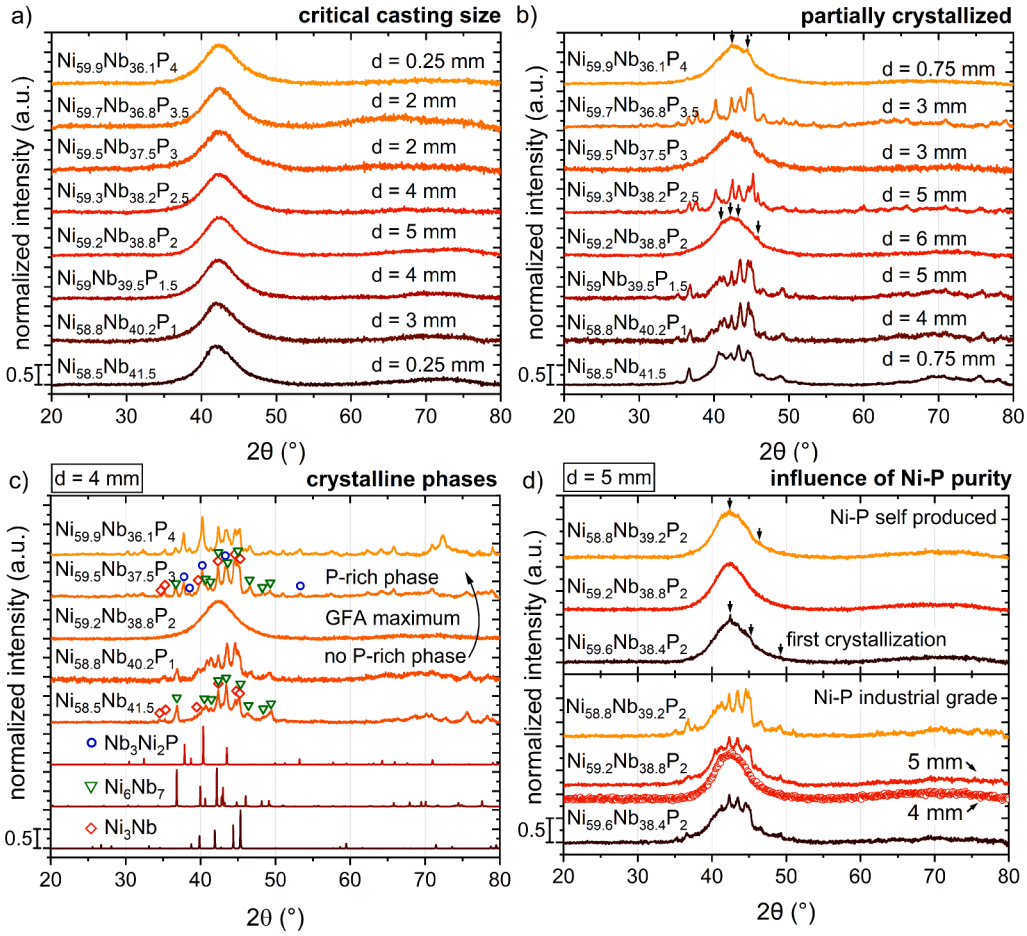

Fig. 1. (a) Critical casting thickness d_c and (b) partially crystallized samples of various sizes of the 'eutectic line' Ni-Nb-P compositions. Plate-shaped specimens were tested for alloys with a critical casting size d_c below 2 mm, while rod-shaped specimens were tested for compositions with a d_c of at least 2 mm. The most significant improvement in glass formation by minor P alloying is found for $Ni_{59.2}Nb_{38.8}P_2$ with a d_c of 5 mm. (c) XRD patterns of 4 mm rods of Ni-Nb-P compositions. In addition to Ni_3Nb and Ni_6Nb_7, the P-rich Nb_3Ni_2P compound emerges as primarily crystallizing phase with increasing P-content. (d) shows the influence of small adjustments of the Ni/Nb ratio on the GFA, as well as the influence of an industrial grade Ni-P master alloy in comparison to the one produced in-house.

composition [48]. The given ideal diffraction patterns of the equilibrium crystalline phases were simulated with the crystallographic data from Ref. [48,49] and [50] for Nb_3Ni_2P, Ni_3Nb and Ni_6Nb_7, respectively. A detailed assignment of the phases is provided in Fig. SI4.

The crystallized samples processed in ESL were subsequently examined by SEM using the BSE contrast and EDX. For binary $Ni_{62}Nb_{38}$ shown in Fig. 2c, the EDX analyses in at% with Ni_{75}-Nb_{25} (Ni_3Nb) for #1 and Ni_{53}-Nb_{47} (Ni_6Nb_7) for #2 are in good agreement with the anticipated crystalline phases, as well as the diffraction data. The slight difference between the measured composition and the actual phase results from the fact that Ni_6Nb_7 is not a strictly stoichiometric compound but has an extensive range of homogeneity in the phase diagram [16]. Both eutectic phases were also detected for the P-rich alloy $(Ni_{62}Nb_{38})_{95}P_5$ in Fig. 2d for #4 and #5 with Ni_{76}-Nb_{24} and Ni_{54}-Nb_{46}, respectively. However, a P-rich phase can additionally be observed with an EDX composition of Ni_{56}-Nb_{24}-P_{20} (Nb_3Ni_2P) for #3. As #3 and #5 display a white contrast in BSE mode, both phases are visually hardly distinguishable, however, their difference in chemical composition from the EDX measurements is significant. This enrichment in P compared to the nominal $(Ni_{62}Nb_{38})_{95}P_5$ composition results from the fact that both crystalline phases Ni_3Nb and Ni_6Nb_7 are completely depleted in P.

Besides the GFA, defining the producibility of amorphous specimens, the thermal stability of the amorphous state against crystallization and its melting behavior are equally important for the processing of BMGs. Commonly, it is characterized upon heating from the glassy state with a rate of 0.333 K s^{-1} from room temperature up to the liquidus temperature. DSC scans of amorphous as-cast samples with increasing P-content were performed as shown in Fig. 3a. All samples crystallize after relaxation into the supercooled liquid region via multiple exothermic reactions. The evolution of the width of the SCLR ΔT_x ($=T_x–T_g$), which also describes the thermal stability against crystallization upon heating is given in the right panel of Fig. 3a. ΔT_x increases continuously with increasing P-content by pushing the first crystallization to higher temperatures. The most thermally stable alloys are observed at $P_{2.5}$ as well as P_3 (ΔT_x=61 K) until ΔT_x declines again at higher P concentrations. Examples for the change of the melting peak are shown for three selected compositions P_1, P_2 and P_3 in Fig. 3b (the rest can be found in Fig. SI5). All samples were molten twice, once starting from an initially amorphous state (solid line), crystallizing during heating and again after the sample crystallized during cooling to serve as a reference (dashed line). The solidus temperature T_m remains almost unaffected by P-additions, whereas the liquidus temperature T_l reveals a strong increase. For instance, P_1 is still close-eutectic due to the proximity to the binary eutectic $Ni_{58.5}Nb_{41.5}$, whereas increasingly higher P contents lead to the appearance of a distinct shoulder. The characteristic temperatures T_g, T_x, T_m, T_l of all glasses in the 'eutectic line' series are summarized in Table 1.

3.2. Glass forming region in the ternary Ni-Nb-P system

All the alloys studied in the ternary Ni-Nb-P compositional space are summarized in Fig. 4a in a color-coded glass-forming map (increasing GFA from red to green). The red squares indicate tested samples with a diameter of 3 mm showing crystalline XRD patterns, followed by the color's orange, yellow and green, where amorphous specimens with a diameter of 3 mm, 4 mm and 5 mm were obtained, respectively. The critical casting size of $Ni_{55}Nb_{40}P_5$ with 2 mm was taken from Ref. [36]. The highest P content tested was 6 at%, however P-contents above 3 at% are already accompanied with a significant drop in GFA. The region of interest with improved GFA, in comparison to binary Ni-Nb, is found at

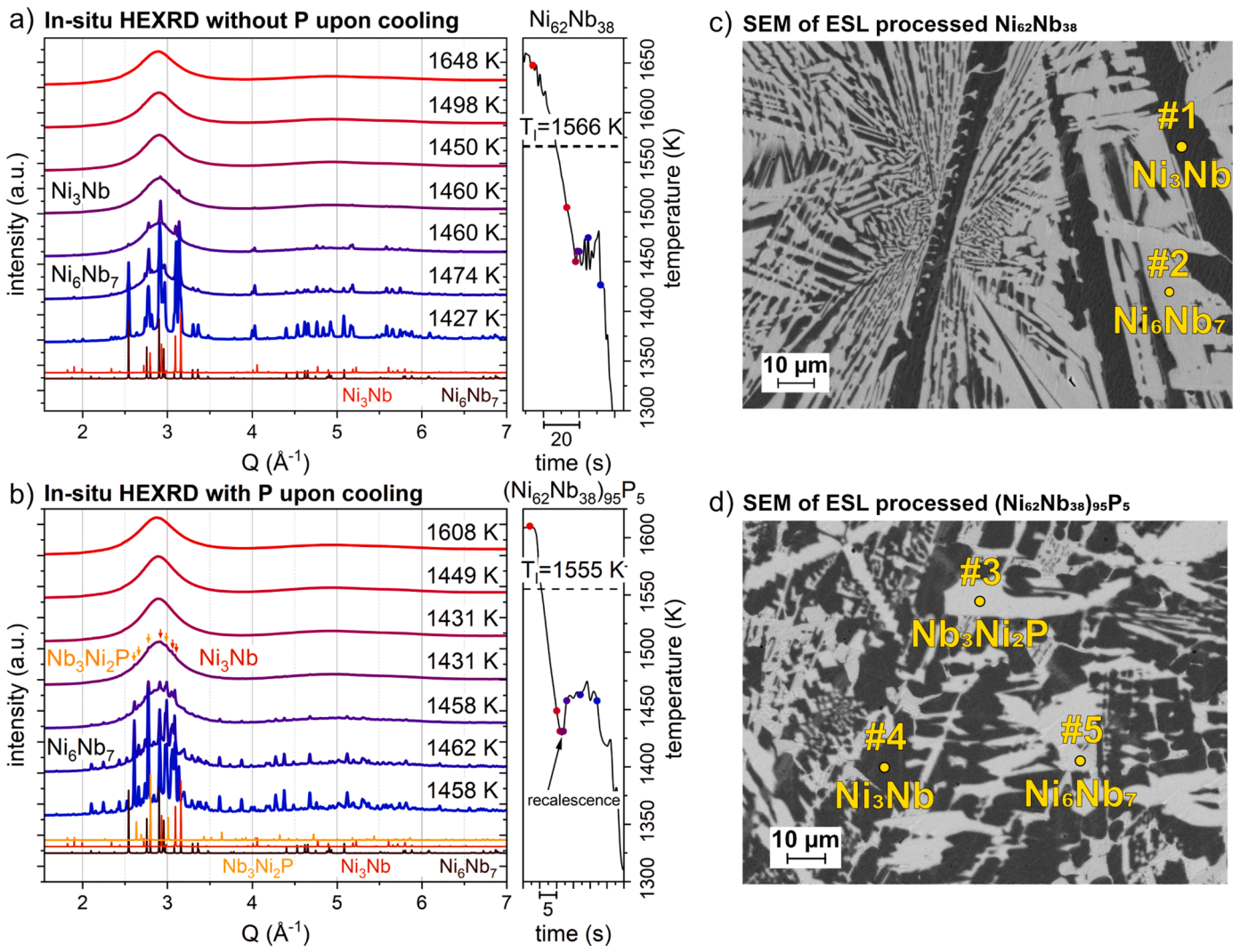

Fig. 2. The left panel depicts the in-situ synchrotron HEXRD patterns of (a) binary $Ni_{62}Nb_{38}$ and (b) $(Ni_{62}Nb_{38})_{95}P_5$ upon cooling from the equilibrium liquid. The right panel shows the corresponding cooling curves. (c) and (d) represent the cross-sectional BSE images of the container less processed ESL samples. The yellow dots indicate the positions at which EDX measurements were performed. The dark phases (#1 and #4) correspond in its composition to Ni_3Nb. The bright phases (#2 and #5) are enriched in Nb with a Ni-Nb ratio close to 1:1, indicating, together with the HEXRD measurements, a Ni_6Nb_7 structure. The second bright phase #3 (hardly distinguishable from #5 in BSE mode, but clearly different in term of EDX composition) corresponds to Nb_3Ni_2P.

contents around 0.5–3 at% P, whereas the alloys with the highest GFA are narrowed down to P-contents around 2 at%. The alloy with the largest critical casting size of 5 mm, $Ni_{59.2}Nb_{38.8}P_2$, was found along the 'eutectic line' and is marked by a green star. Fig. 4b depicts the DSC scan of a 5 mm amorphous cylindrical sample, showing the typical heat capacity step from the glassy state to the SCL, followed by multiple crystallization events. Compared to initially eutectic melting of $Ni_{58.5}Nb_{41.5}$, a pronounced melting shoulder appears, increasing the liquidus temperature to 1517 K. The inset represents a typical room temperature HEXRD synchrotron pattern (raw picture and integrated curve) without the appearance of any crystalline Bragg-peaks. Moreover, the crystallization enthalpy ΔH_x of the 5 mm sample is equal to the fully amorphous one tested in Fig. 3a ($\Delta H_x^{5\ mm} = \Delta H_x^{3\ mm} = -5.4$ kJ g-atom^{-1}), proving the amorphous structure of 5 mm as-cast $Ni_{59.2}Nb_{38.8}P_2$. In summary, minor additions of P allow an increase in GFA from 2 mm (0.25 mm) for binary $Ni_{62}Nb_{38}$ ($Ni_{58.5}Nb_{41.5}$) up to 5 mm for ternary Ni-Nb-P, which to our knowledge has to date not been reported in the literature for Ni-Nb based alloys.

3.3. *Ni-Nb-Ta-P system – alloy optimization by substitution of Nb with Ta*

Various thicknesses of $Ni_{59.2}Nb_{38.8-y}Ta_yP_2$ (hereafter Ta_y, y=0, 1, 3, 5, …, 38.8) were studied, indicating a rise of the critical casting thickness up to 6 mm over a wide range from 1 to 13 at% Ta until a continuous decrease to 4, 3 and 2 mm sets in, as shown in Fig. 5a. Unlike the narrow GFA window in the Ni-Nb system upon P-addition, the $Ni_{59.2}Nb_{38.8-x}Ta_xP_2$ series appear to be robust to compositional changes between Nb and Ta due to their similar topological and chemical properties. The very same 6 mm X-ray amorphous samples shown in Fig. 5 were additionally measured at room temperature with high energy synchrotron radiation, revealing the occurrence of a minor crystalline fraction in most of the samples (Fig. 5b). However, Ta_5 possesses a HEXRD pattern without Bragg-peaks, revealing its fully amorphous structure. Consequently, the GFA in the Ni-Nb-Ta-P quaternary is 1 mm higher than that of the Ni-Nb-P ternary (d_c of 5 mm). The analysis of 7 mm cylindrical rods around Ta_5 proves that this composition is indeed the one with the highest GFA, exhibiting a mostly amorphous XRD pattern superimposed by first crystallization. The alloys compositionally next to it precipitate the Nb_3Ni_2P, Ni_6Nb_7 and Ni_3(Nb,Ta) compounds.

Based on DSC measurements, the crystallization enthalpy ΔH_x can be

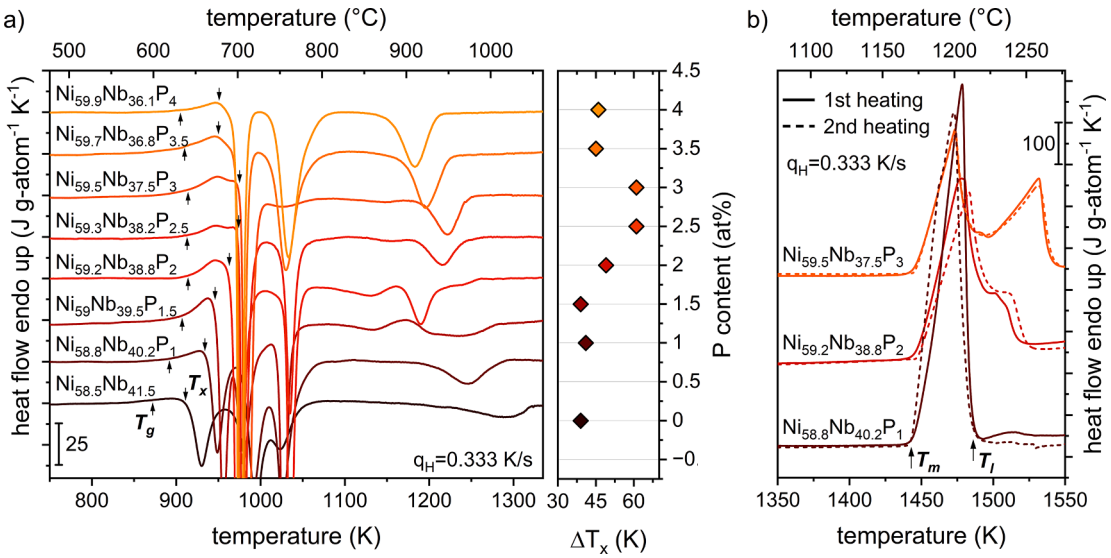

Fig. 3. (a) Left panel: DSC scans at 0.333 K s^{-1} of the 'eutectic line' series in the ternary Ni-Nb-P system for fully amorphous samples. T_g and T_x are indicated with an arrow. Right panel: Progression of the width of the supercooled liquid region ΔT_x (=T_x-T_g) as a function of the P content. (b) Melting curves of P_1, P_2 and P_3 measured from an initially amorphous (solid lines) and crystalline state (dashed lines).

Table 1
Characteristic parameters determined by DSC measurements at a heating rate q_H of 0.333 K s^{-1} of the 'eutectic line' compositions, including the series with the addition of Ta. T_g, T_x, T_m and T_l corresponds to the onset of the glass transition, onset of crystallization as well as melting and liquidus temperature, respectively. ΔT_x (=T_x-T_g) represents the width of the SCLR and T_{rg} (=T_g/T_l) the reduced glass transition temperature. The critical casting thickness was determined by XRD measurements. Some of the Ta-containing alloys have a d_c of about 6 mm, as high energy synchrotron X-ray analysis revealed a minor crystalline fraction.

Composition (at%)	T_g (K)	T_x (K)	T_m (K)	T_l (K)	ΔT_x (K)	T_{rg}	d_c (mm)
$Ni_{58.5}Nb_{41.5}$	872	911	1453	1492	39	0.584	0.25
$Ni_{58.8}Nb_{40.2}P_1$	892	933	1444	1486	41	0.600	3
$Ni_{59}Nb_{39.5}P_{1.5}$	907	946	1444	1510	39	0.601	3
$Ni_{59.2}Nb_{38.8}P_2$	914	963	1447	1517	49	0.603	5
$Ni_{59.3}Nb_{38.2}P_{2.5}$	913	974	1446	1527	61	0.598	4
$Ni_{59.5}Nb_{37.5}P_3$	914	975	1446	1540	61	0.594	2
$Ni_{59.7}Nb_{36.8}P_{3.5}$	905	950	1444	1547	45	0.585	2
$Ni_{59.9}Nb_{36.1}P_4$	905	951	1442	1558	46	0.581	0.25
$Ni_{59.2}Nb_{37.8}Ta_1P_2$	913	964	1447	1516	51	0.602	~6
$Ni_{59.2}Nb_{35.8}Ta_3P_2$	914	971	1453	1521	57	0.601	~6
$Ni_{59.2}Nb_{33.8}Ta_5P_2$	917	977	1459	1527	60	0.601	6[a]
$Ni_{59.2}Nb_{31.8}Ta_7P_2$	927	988	1468	1539	61	0.602	~6
$Ni_{59.2}Nb_{29.8}Ta_9P_2$	933	994	1473	1545	61	0.604	~6
$Ni_{59.2}Nb_{27.8}Ta_{11}P_2$	934	999	1478	1553	65	0.601	~6
$Ni_{59.2}Nb_{25.8}Ta_{13}P_2$	939	1003	1485	1558	64	0.603	~6
$Ni_{59.2}Nb_{23.8}Ta_{15}P_2$	941	1010	1493	1565	69	0.601	4
$Ni_{59.2}Nb_{18.8}Ta_{20}P_2$	948	1017	1506	1581	69	0.600	4
$Ni_{59.2}Nb_{13.8}Ta_{25}P_2$	959	1028	1534	1609	68	0.596	3
$Ni_{59.2}Nb_{8.8}Ta_{30}P_2$	972	1039	1565	1641	67	0.592	3
$Ni_{59.2}Ta_{38.8}P_2$	989	1051	1627	1684	62	0.587	2

[a] mostly amorphous 7 mm XRD pattern.

determined as shown in Fig. 5d and the amorphous fraction can be estimated. Within the limits of measurement accuracy, the 6 mm HEXRD amorphous alloy Ta_5 exhibits approximately the same crystallization enthalpy of −6 kJ g-atom^{-1} as a 4 mm rod of the same composition with −6.1 kJ g-atom^{-1}. In contrast, the mostly XRD amorphous 7 mm specimen with first appearance of crystalline fraction reveals a slightly lower ΔH_x of −5.5 kJ g-atom^{-1}. Assuming ΔH_x correlates with the volumetric proportion of the amorphous phase in a first approximation, the 7 mm rod is about 91 % amorphous.

Fig. 6 shows the DSC curves of $Ni_{59.2}Nb_{38.8-y}Ta_yP_2$ (y=0, 1, 3, 5, …, 38.8) amorphous specimens, exhibiting a distinct glass transition, followed by a supercooled liquid region prior to crystallization. With increasing Ta content, T_g as well as solidus T_m and liquidus temperature T_l increase continuously due to the very high melting temperature of pure Ta (3020 °C [51]). For instance, the glass transition temperature of P_2 (y=0) was determined to be 914 K at a heating rate of 0.333 K s^{-1}, while a full substitution with Ta (y=38.8) results in a 75 K higher T_g of 989 K. Accordingly, the intermediate alloy compositions containing both, Nb and Ta, exhibit a T_g in between. As can be seen from the right panel of Fig. 6a, ΔT_x, as the width of the SCLR, increases steadily upon Ta addition from initially 49 K for the base alloy P_2 to a maximum of 69 K between Ta_{15} to Ta_{20} before dropping to 62 K for the ternary composition without Nb, $Ni_{59.2}Ta_{38.8}P_2$. As shown in Fig. 6b, T_m and T_l increase even more from 1447 K to 1627 K and from 1520 K to 1684 K, respectively. In the case of complete Nb substitution, the proximity of $Ta_{38.8}$ to the binary eutectic $Ni_{63.8}Ta_{36.2}$ results in near-eutectic melting. A detailed overview of all melting curves are given in Fig. SI6 and the characteristic temperature values of the entire Ta-series are listed in Table 1. Moreover, it should be noted that the alloys with a large SCLR show an anomalous exothermic peak in the SCLR, which is reminiscent of a double glass transition. Similar effect was observed by Na et al. upon Ta addition in Ni-Zr-based alloys, which were attributed to the formation of a distinct medium range order [52]. However, further studies are needed to understand this phenomenon in detail.

3.4. Mechanical properties – ultra high strength BMGs with high GFA

Metallic glasses are generally microscopically (intrinsically) ductile and undergo shearing at an angle of about 45° near the direction of maximum resolved shear stress in tensile tests. However, the fracture behavior is mainly determined by a single, highly localized shear band that fractures catastrophically, resulting in negligible tensile elongation [53]. Therefore, the mechanical properties of amorphous metals are usually assessed by compression tests, which can promote the formation of multiple shear bands and extensive plastic flow for samples with sufficient intrinsic ductility. Fig. 7 presents the compressive stress-strain curves of the best glass forming compositions in the binary, ternary and quaternary Ni-Nb system. All alloys exhibit an elastic strain of about 2 %, a Young's modulus between 124 and 145 GPa, and yielding at high stresses in the range of 3 GPa, followed by plastic deformation with serrated flow behavior. The total strain is increased on average by about

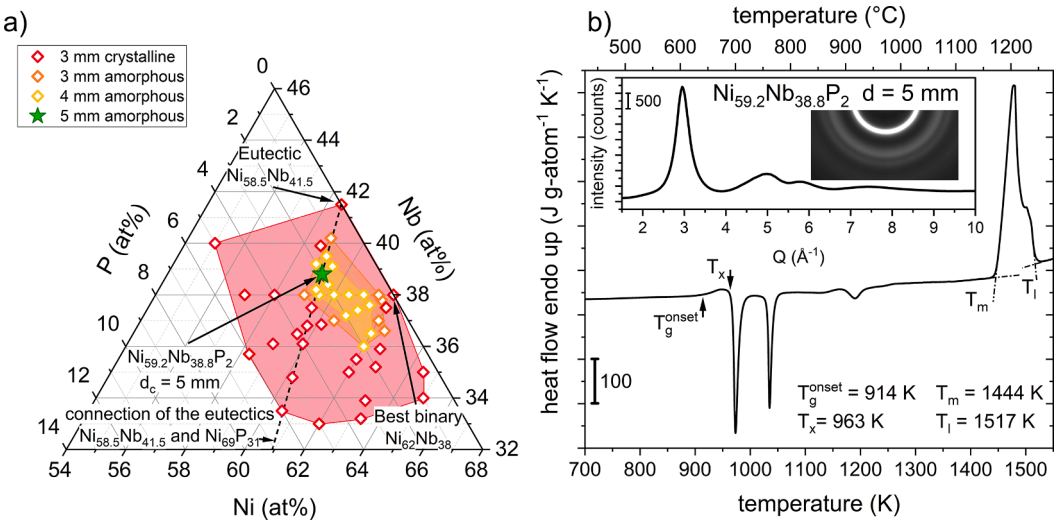

Fig. 4. (a) Magnified ternary Ni-Nb-P GFA map of the investigated compositional space shows a wide range in which the GFA could be increased from 2 mm (GFA of the best binary composition $Ni_{62}Nb_{38}$) up to 3 mm (orange area) and 4 mm (yellow area). The alloy with the highest critical casting thickness of 5 mm is marked by a green star. (b) DSC scan at 0.333 K s^{-1} of a 5 mm rod of the best found glass former $Ni_{59.2}Nb_{38.8}P_2$ in the ternary Ni-Nb-P system. The HEXRD inset verifies the amorphous structure of the 5 mm sample cut from the very same rod.

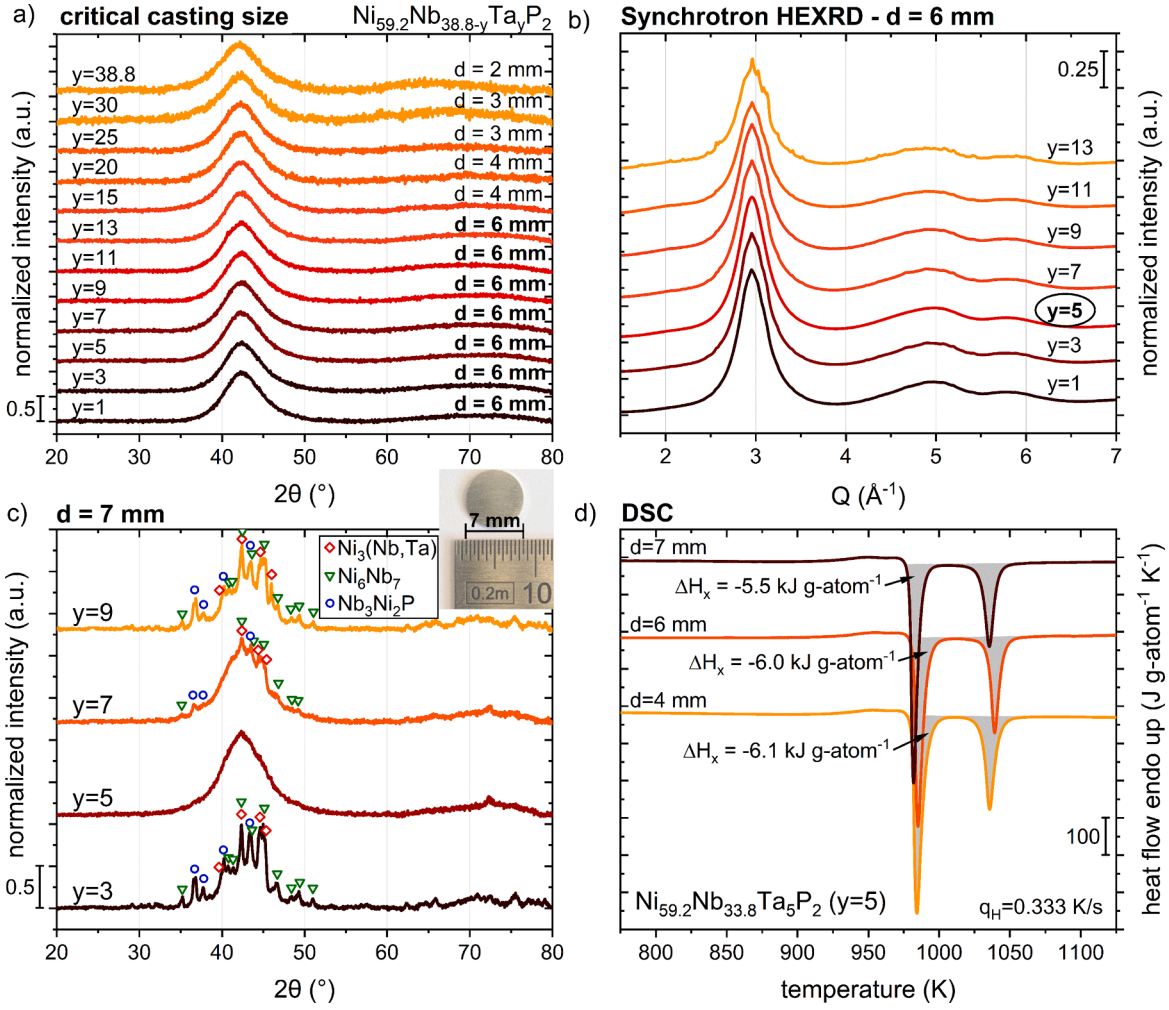

Fig. 5. (a) Critical casting thickness of the $Ni_{59.2}Nb_{38.8-y}Ta_yP_2$ series up to a complete substitution of Nb by Ta. (b) In depth high energy synchrotron radiation experiments reveal that only Ta_5 (y=5) is fully synchrotron amorphous. The rest depicts small amounts of crystalline Bragg peaks. (c) Testing around the amorphous composition (y=5) reveals that this is indeed the best quaternary alloy with a critical diameter of almost 7 mm. The inset shows the 7 mm specimen examined. (d) The presence of small crystalline fractions in the 7 mm rod is also observed by DSC in form of less released crystallization enthalpy.

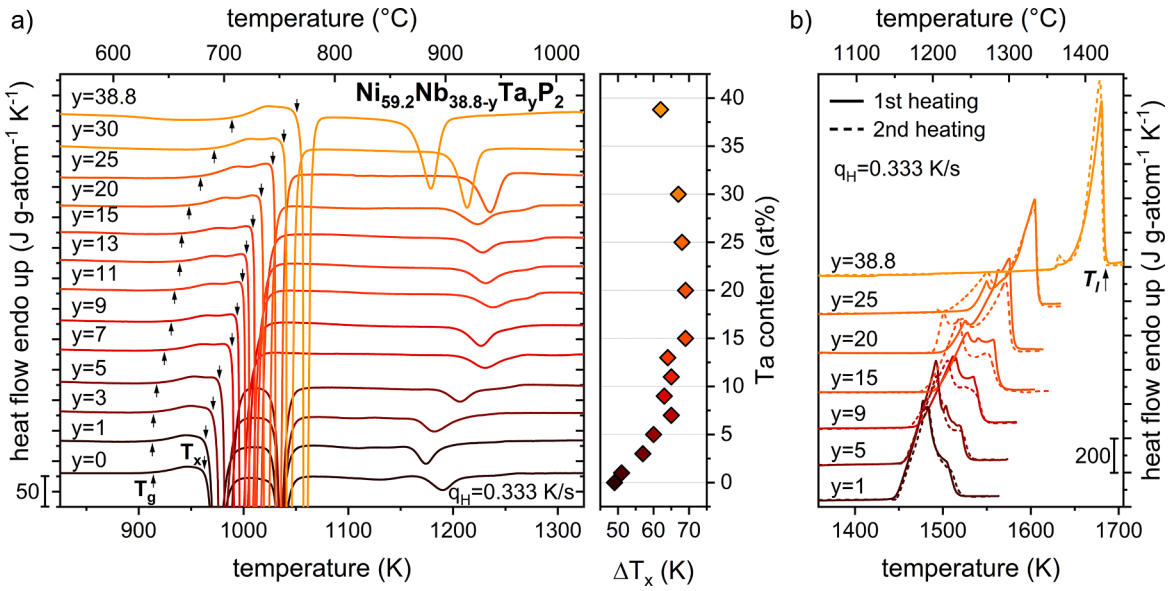

Fig. 6. (a) Left panel: DSC scans at 0.333 K s^{-1} of $Ni_{59.2}Nb_{38.8-y}Ta_yP_2$ (y = 0, 1, 3, 5, …, 38.8) of fully amorphous samples. The last one represents a complete substitution of Nb by Ta. Right panel: Evolution of the width of the supercooled liquid region ΔT_x ($=T_x$-T_g) upon Nb substitution by Ta. (b) Some representative melting curves for different Ta contents measured from an initially amorphous (solid lines) and crystalline state (dashed lines).

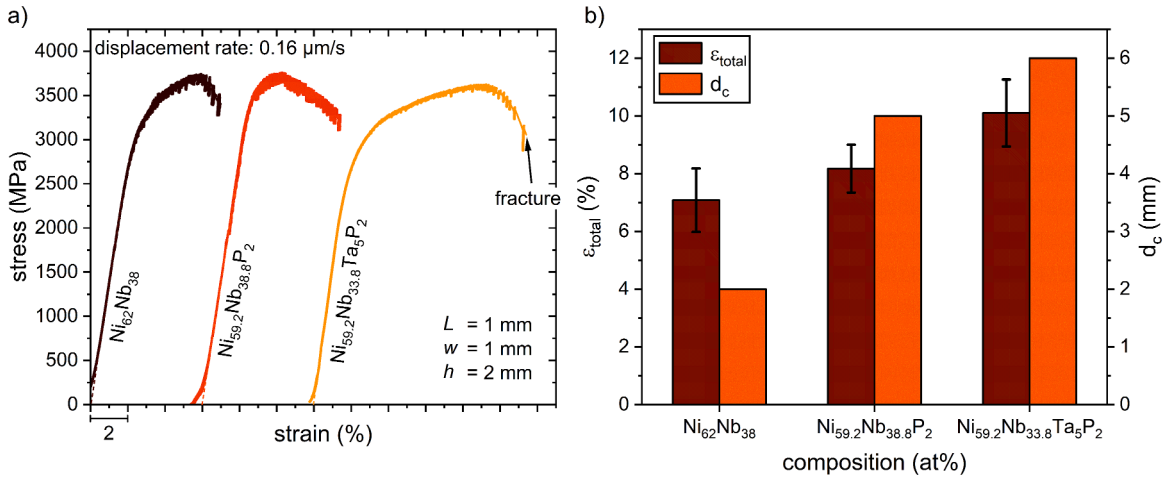

Fig. 7. (a) Engineering stress-strain curves of two Ni-Nb-(Ta)-P alloys developed in this work in comparison to binary $Ni_{62}Nb_{38}$. For good statistics, five to six rectangular shaped beams of each composition with the nominal dimensions of 1×1×2 mm^3 (L×w×h) were tested in compression experiments. (b) shows the evolution of the total strain to failure as well as the critical casting thickness d_c.

0.5 % from $Ni_{62}Nb_{38}$ to $Ni_{59.2}Nb_{38.8}P_2$ upon P addition and again about 2 % upon Ta addition. Moreover, the stress increases after yielding, which is unusual for amorphous metals, as they usually exhibit the phenomenon of strain softening rather than strain hardening. The latter effect is most pronounced in the quaternary alloy $Ni_{59.2}Nb_{33.8}Ta_5P_2$ with an average strain to failure of ~10 %. A detailed summary of the mechanical properties and their standard deviations obtained from compression tests are provided in Table 2.

Table 2
Mechanical properties of the novel Ni-Nb-(Ta)-P alloys developed in this work in comparison to binary Ni-Nb. E corresponds to the Youngs modulus, σ_y to the yield strength, σ_u to the ultimate compression strength, ε_{total} to the total strain to failure calculated from the compression stress-strain curves. *HV5* corresponds to the Vickers hardness, measured with an indentation force of 49.03 N.

Composition (at%)	E *(GPa)*	σ_y (GPa)	σ_u (GPa)	ε_{total} (%)	*HV5*
$Ni_{62}Nb_{38}$	124±4	2.96±0.15	3.39±0.09	7.7±1.1	862±11
$Ni_{59.2}Nb_{38.8}P_2$	145±7	3.35±0.17	3.72±0.05	8.2±0.8	887±7
$Ni_{59.2}Nb_{33.8}Ta_5P_2$	142±8	2.85±0.08	3.46±0.10	10.1±1.2	892±12

Hardness measurements of the glassy $Ni_{62}Nb_{38}$ and $Ni_{59.2}Nb_{38.8}P_2$ alloys show that minor P additons lead to an increase in the hardness from 862 to 887 HV5, respectively. Further alloying of Ta up to a complete substitution of Nb is depicted in Fig. 8. Starting from 887 HV5 for P_2, the hardness increases linearly with rising Ta content up to about 1000 HV5 (989±14 HV5) for $Ta_{38.8}$. As summarized in Table 1, the addition of high-melting point Ta leads to a continuous increase in the glass transition and liquidus temperature, causing that improvement in hardness. This is primarily related to the general correlation between those two properties, as high melting elements are usually harder [54]. From this wide range of alloys with high GFA (2 mm to 6 mm), the most suitable candidate in terms of hardness can be selected for each application.

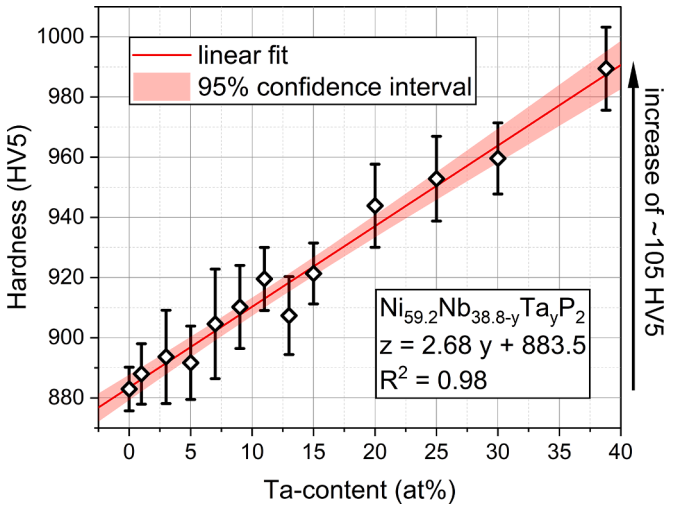

Fig. 8. Hardness (HV5) evolution as a function of the Ta content of $Ni_{59.2}Nb_{38.8-y}Ta_yP_2$ (y=Ta content) alloys up to a complete substitution of Nb by Ta, which proceeds linearly upon Ta addition.

4. Discussion

Ni-Nb as one of the best binary metallic glass forming systems possesses exceptional mechanical properties and is therefore highly promising for potential industrial applications, competing with high performance steels (e.g. HSS, TRIP and TWIP steels) [12,55]. For a stable and robust casting process utilizing water-cooled metallic molds, it is essential to elevate the GFA well above the 2 mm threshold of the binary system. Metalloids are generally favorable candidates to impede crystallization, since they exhibit a strong negative enthalpy of mixing ΔH_{mix} with many metallic elements such as P in the Ni-Nb system with ΔH_{mix}^{Ni-P} of −34.5 kJ mol^{-1} and ΔH_{mix}^{Nb-P} of −89.5 kJ mol^{-1} [56]. Moreover, P has a very small atomic radius of 106 pm, compared to Ni and Nb with 126 pm and 150 pm, respectively [57]. This combination of strong negative ΔH_{mix} and mismatch of small, medium and large atoms can increase the packing density in the melt and ultimately favor glass formation [58]. Similar behavior is observed for other metalloid elements such as Si, S, C and B [29,59-61], which on the one hand promote efficient packing of the atoms, but on the other hand form compounds with high melting temperatures, which in turn can be detrimental for the GFA [31,61,62]. For instance, Bochtler et al. discovered that crystallization in a sulfur-containing Zr-based BMG (Vit105S_2) is triggered earlier by the formation of an S-rich intermetallic phase compared to the alloy without S [63]. In the Ni-Nb system, a change of the primary phase also takes place upon micro-alloying with P, here from Ni_3Nb to the P-rich intermetallic phase Nb_3Ni_2P. The EDX analysis from the ESL processed $(Ni_{62}Nb_{38})_{95}P_5$ alloy revealed that the solubility of P in the primary Ni_3Nb phase approaches zero (see Fig. 2), necessitating P diffusion and redistribution for its formation. The same applies to Nb_3Ni_2P, although local enrichment of P in the supercooled melt is required for its formation. This indicates that nucleation of primary Ni_3Nb is restricted for low concentrations up to 2 at% P, since compositional fluctuations required to form critical nuclei are more difficult to realize. However, excessive P alloying (>2 at% P) triggers the formation of the P-rich phase, which in turn is detrimental for glass formation. Thus, about 2 at% P seems to be the optimum to retard the precipitation of Ni_3Nb, but not yet to form the high-melting intermetallic P-rich phase. An additional contribution to the improved GFA in the range of 2 at% might be the slowdown of the kinetics of the glass and liquid, as indicated by the continuous increase in T_g.

As can be seen in Fig. 3 (or Table 1), the thermal stability ΔT_x increases with increasing P content, which might be connected to the highly negative enthalpy of mixing with the other constituents. In general, minor additions stabilizing the SCLR are widely reported in literature, e.g., by Sn [12] or S [64] in the case of Ni-Nb alloys. However, the thermal stability correlates poorly with the GFA, as it describes the stability of a deeply supercooled liquid against crystallization and not the resistance against nucleation upon cooling from the equilibrium liquid. Such a poor correlation is frequently reported in Ti-based bulk glass-forming alloys, exhibiting almost no SCLR despite their high GFA due to the nucleation of a quasi-crystalline icosahedral phase upon heating [42,65]. In contrast, the reduced glass transition temperature T_{rg} closely mirrors the course of d_c as depicted along with the evolution of T_g and T_l in Fig. 9. Despite the growth of a distinct melting shoulder upon P addition (see Fig. 3b), the continuous increase of T_l is not detrimental for glass formation in the range of 0–2 at% P, as T_g rises even more, leading to vitrification at higher temperatures. This ultimately reduces the temperature range (T_l-T_g), that must be bypassed for vitrification, resulting in a high T_{rg} value of 0.603 for P_2. The subsequent decline of T_{rg} along with the GFA beyond 2 at% is dominated by the increase of the liquidus temperature, while T_g hardly changes. This interplay between T_g and T_l is best reflected by the classical GFA parameter T_{rg}, as below T_l there is a driving force for crystallization, while T_g marks the point of vitrification of a liquid into a solid. In summary, micro-alloying proves once again that it is a powerful tool to promote glass formation. However, detailed studies on the thermodynamic, topological, and chemical aspects are required for a more comprehensive understanding of the phenomena of minor alloying in this system.

Further alloy development was done by stepwise substitution of Nb by Ta up to a complete replacement. From a structural point of view, the atomic radii of both elements are similar (r^{Nb}=150 pm and r^{Ta}=154 pm) and can be considered as topological equivalent [57]. Furthermore, both are chemically very similar with a neutral enthalpy of mixing ΔH_{mix}^{Nb-Ta} of 0 kJ mol^{-1} [56]. Originally, Nb and Ta were even considered as one element 'columbium', until it could be proven in the 19th century that they are actually two different ones [66]. This already demonstrates their very similar characteristics, which are also evident in the binary phase diagram, as Nb-Ta forms a solid solution over the entire compositional range, indicating good compatibility between the two elements [67]. In combination with Ni, a deep eutectic forms at $Ni_{63.8}Ta_{36.2}$, which is compositionally close to the $Ni_{59.5}Nb_{40.5}$ eutectic [16,51]. Consequently, it is not surprising that binary Ni-Ta also belongs to one of the best-known binary BMGs with a critical diameter of 2 mm, analogous to binary Ni-Nb [18,68].

Moreover, Ta does not seem to influence the crystalline phases

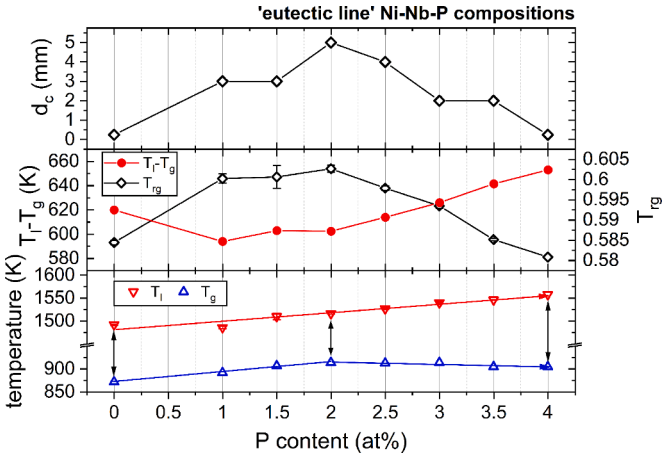

Fig. 9. Correlation of the critical casting thickness d_c, the reduced glass transition temperature T_{rg}, the glass transition temperature T_g and the liquidus temperature T_l of the 'eutectic line' Ni-Nb-P compositions. The temperature range between T_l and T_g, that must be bypassed for vitrification, is among the lowest for P_2, coinciding with the observed maximum of T_{rg} and d_c.

competing with glass formation, which might be connected to the fact that both systems (Ni-Nb [16] and Ni-Ta [51]) form the same complex intermetallic phases with orthorhombic Ni_3Nb and Ni_3Ta as well as trigonal Ni_6Nb_7 and NiTa. Hence, the formation of higher ordered compounds does not occur, which would be detrimental for the GFA. The phases Nb_3Ni_2P, Ni_6Nb_7 and Ni_3(Nb,Ta) were assigned (see Fig. 5d), whereas the latter can be interpreted as two distinct phases Ni_3Nb and Ni_3Ta or as mixture of both intermetallic phases, as they share the same orthorhombic unit cell structure. Hence, it is likely that some of the Nb positions are occupied by Ta. Considering Vegard's law, the orthorhombic mixture Ni_3(Nb,Ta) can be simulated, revealing no significant differences compared to ideal Ni_3Nb and Ni_3Ta diffractograms, despite a slight shift in peak positions (Fig. SI7). However, the crystalline phases observed in the samples produced by copper mold casting are usually supersaturated phases due to the very high cooling rates, which also causes a shift of the Bragg peaks. Therefore, it is uncertain whether the individual phases are present or a mixed phase, as a precise assignment is not possible. Nevertheless, it is evident from the ternary phase diagram that Ni_3Ta must be present in some form with increasing Ta content [69]. In conclusion, Ta addition in the range of 1 to 13 at% does not have a pronounced capability to frustrate crystallization and the improvement of the GFA from 5 to 6 mm is likely connected to a higher number of elements, leading to an ascending complexity of the liquid, satisfying the empirical rules for glass formation [30]. Thus, it is surprising that the critical diameter above 13 at% decreases down to 2 mm for $Ni_{59.2}Ta_{38.8}P_2$, which is substantially lower compared to off-eutectic $Ni_{59.2}Nb_{38.8}P_2$ (d_c of 5 mm). This might imply that micro-alloying of P is less effective in the Ni-Ta-P system, as the GFA is comparable to binary Ni-Ta alloys [20]. However, the ternary Ni-Ta-P system was not adjusted and optimized for its P content, as well as the Ni and Ta content. Hence, targeted alloy optimization in the ternary Ni-Ta-P system with the aim of producing BMGs with even more extreme properties (e.g., high T_g, yield strength and hardness) is a promising approach for future studies.

In comparison to the ternary $Ni_{59.2}Nb_{38.8}P_2$ base alloy, the thermal stability could be improved by 20 K up to 69 K by introducing 15–20 at% Ta into the system. Such a stable SCLR is a key feature for processing techniques like thermoplastic forming or selective laser melting. T_{rg} on the other hand is fairly constant between Ta_1 to Ta_{13} ranging from 0.601-0.604, matching with the wide glass forming region in which 6 mm XRD amorphous samples were found, which is shown in detail in Fig. 10 along with the trends in the glass transition and liquidus temperatures. Both properties, T_g and T_l, follow a linear trend in a comparable manner up to 15 at% Ta. Beyond that, T_l rises proportionally stronger than T_g, which is visible from the change in slope. Focusing on

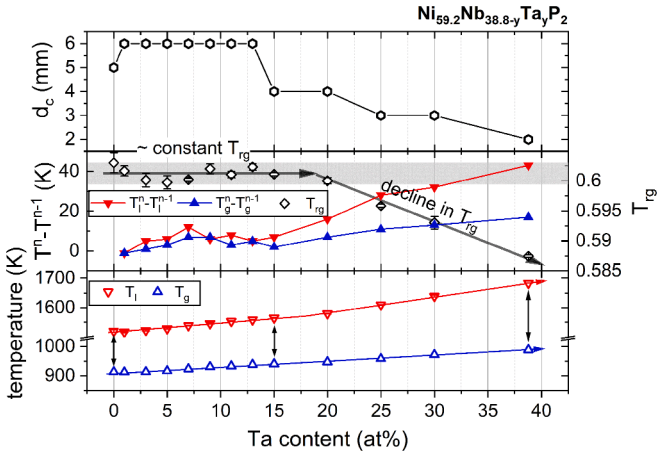

Fig. 10. Correlation between liquidus temperature T_l, glass transition temperature T_g, GFA criterion T_{rg} and the critical casting size d_c for $Ni_{59.2}Nb_{38.8-y}Ta_yP_2$ (y=0, 1, 3, 5, ..., 38.8) bulk metallic glasses. T^n-T^{n-1} represents the change of T_g or T_l to the value of the previous composition.

the increase of T_g and T_l from alloy to alloy (T^n-T^{n-1}), both temperatures increase nearly identically by 5–12 K between 1 and 13 at% Ta. Consequently, T_{rg} (=T_g/T_l) remains approximately constant in this compositional range, analogous to the critical casting thickness d_c. The subsequent decline in d_c and in the GFA parameter T_{rg} is accompanied by the divergence of the liquidus and glass transition temperatures. This suggests that the GFA of the Ta-rich alloys (>15 at% Ta) can be potentially improved by lowering the liquidus temperature, as T_g is relatively insensitive to small compositional changes.

Due to their amorphous structure, metallic glasses commonly exhibit a uniform microstructure and thus exhibit shear softening as deformation is usually located in a single shear band [53]. However, different works show that adding small amounts of elements with positive enthalpy of mixing can cause a microstructural heterogeneity, which can impede the easy propagation of shear bands and ultimately promote multiple shear band formation [70–72]. However, this cannot be the case for P and Ta addition, as they mainly possess a negative enthalpy of mixing (neutral ΔH_{mix} for Nb-Ta) with the constituent atoms. Furthermore, the $Ni_{62}Nb_{38}$ alloy features strain hardening, which indicates a nanometer scale heterogeneity already in the binary system. This is supported by the structural study of Lu et al. who found a chain-like network structure of interpenetrating icosahedral clusters beyond the nearest neighbor distance in binary Ni-Nb [73]. The structural heterogeneity is believed to be the origin of the high GFA and might be the explanation for the observed strain hardening effect in this work. In general, the improved compressive ductility in the ternary system is surprising as minor additions (of metalloids) usually cause an embrittlement in many different systems. For instance, Garrett et al. associated the decrease in toughness by micro-alloying with an increase in glass transition temperature and yield strength, all properties that also increase in $Ni_{59.2}Nb_{38.8}P_2$ [74]. In case of the Ni-Nb-Ta-P system, the findings by Johnson et al. indicate that elements increasing the glass transition temperature T_g can raise the activation barrier for shearing, which results in alloys with higher Ta content (and thus higher T_g) being more prone to brittle deformation, as the formation of shear bands is impeded [75]. However, such an embrittlement cannot be observed here, which might be connected to the ascending complexity of the system and consequently an increased heterogeneity, which contributes to multiple shear band formation. Another contributing factor may be that all compression samples were cast with a maximum dimension of 2 mm, which is approximately equal to d_c for the Ni-Nb BMG, and progressively farther from d_c for the Ni-Nb-P and Ni-Nb-Ta-P BMGs, respectively. This means that the P_2 and Ta_5 are cast into progressively more rejuvenated energy states compared to the $Ni_{62}Nb_{38}$ BMG, and higher energy states are well known to promote ductility in BMGs [76]. However, further analysis is required to fully understand the mechanical behavior of these new alloys, which was not the main scope of the initial characterization carried out in this study.

5. Conclusion

With the aim of improving one of the best binary glass formers $Ni_{62}Nb_{38}$ in terms of GFA, while maintaining its excellent mechanical properties, minor amounts of P were introduced to the Ni-Nb-P system. Further optimization of Nb substitution by Ta in the Ni-Nb-Ta-P system on the GFA, thermal stability and compressive mechanical properties were also investigated. The results are summarized as follows:

- Micro-alloying of P elevated the GFA from 2 mm for binary Ni-Nb to 5 mm for $Ni_{59.2}Nb_{38.8}P_2$. Further improvement was achieved by substituting Nb with Ta, leading to a critical casting diameter of 6 mm for $Ni_{59.2}Nb_{33.8}Ta_5P_2$ with the potential for an even higher GFA of 7 mm, which can be likely achieved by further alloy optimization or the introduction of further appropriate elements.

- In-situ HEXRD experiments indicate that a drop in GFA beyond 2 at% P is connected to the formation of a P-rich intermetallic Nb_3Ni_2P phase.
- Furthermore, both P and Ta additions significantly enlarged the supercooled liquid region ΔT_x up to a maximum of 69 K.
- Both improvements of GFA and thermal stability are believed to be achieved by fulfilling the three empirical rules for glass formation, in particular by the large negative heat of mixing of P and the size mismatch to the main constituents brought in by P as well as Ta, which favors an efficient packing of atoms.
- Along with a high yield strength ($\sigma_y \approx 3$ GPa), both the binary $Ni_{62}Nb_{38}$ and ternary $Ni_{59.2}Nb_{38.8}P_2$ samples exhibit a significant strain to failure of 7–8 %, while the total compressive strain of the quaternary $Ni_{59.2}Nb_{33.8}Ta_5P_2$ samples reached 10 %. Moreover, Vickers hardness of 860–1000 HV5 were achieved.

In summary, micro-alloying of P tremendously enhances the GFA and thermal stability in the Ni-Nb system while maintaining the excellent mechanical properties, paving the way for its application as structural materials.

Declaration of Competing Interest

The authors declare that they have no known competing financial interests or personal relationships that could have appeared to influence the work reported in this paper.

Acknowledgments

The authors would like to thank F. Aubertin, I. Gallino and A. Kuball for many fruitful discussions. We also thank DESY (Hamburg, Germany) for providing the experimental facilities. Parts of this research were performed at PETRA III at the P21.2 beam facility, and we would like to thank Malte Blankenburg and Ulrich Lienert for their support. Furthermore, we would like to thank the German Aerospace Center (DLR) for providing the electrostatic levitator setup for the in-situ synchrotron diffraction experiments, especially Dirk Holland-Moritz, Johanna Wilden, Lucas Kreuzer and Nicolai Grund who assisted during the campaign. This research was partially supported by the German Research Foundation (DFG) through Grant No. BU 2276/11-1 and No. ME 1958/12-1. Moreover, instrumentation and technical assistance for this work were provided by the Service Center X-ray Diffraction, with financial support from Saarland University and German Science Foundation (project number INST 256/349-1). The authors thank Dr. Oliver Janka for the support in collection of the X-ray diffraction data presented in this paper.

Supplementary materials

Supplementary material associated with this article can be found, in the online version, at doi:10.1016/j.actamat.2023.118968.

References

[1] A.L. Greer, E. Ma, Bulk metallic glasses: at the cutting edge of metals research, MRS Bull. 32 (08) (2007) 611–619, https://doi.org/10.1557/mrs2007.121.
[2] M. Telford, The case for bulk metallic glass, Mater. Today 7 (3) (2004) 36–43, https://doi.org/10.1016/S1369-7021(04)00124-5.
[3] R. Busch, The thermophysical properties of bulk metallic glass-forming liquids, JOM 52 (7) (2000) 39–42, https://doi.org/10.1007/s11837-000-0160-7.
[4] R. Busch, J. Schroers, W.H. Wang, Thermodynamics and kinetics of bulk metallic glass, MRS Bull. 32 (8) (2007) 620–623, https://doi.org/10.1557/mrs2007.122.
[5] R. Busch, I. Gallino, Kinetics, thermodynamics, and structure of bulk metallic glass forming liquids, JOM 69 (11) (2017) 2178–2186, https://doi.org/10.1007/s11837-017-2574-5.
[6] C.C. Hays, et al., Vitrification and determination of the crystallization time scales of the bulk-metallic-glass-forming liquid $Zr_{58.5}Nb_{2.8}Cu_{15.6}Ni_{12.8}Al_{10.3}$, Appl. Phys. Lett. 79 (11) (2001) 1605–1607, https://doi.org/10.1063/1.1398605.
[7] J.H. Na, M.D. Demetriou, M. Floyd, A. Hoff, G.R. Garrett, W.L. Johnson, Compositional landscape for glass formation in metal alloys, Proc. Natl. Acad. Sci. 111 (25) (2014) 9031–9036, https://doi.org/10.1073/pnas.1407780111.
[8] H. Jiang, et al., Effect of sulfur on the glass-forming ability, phase transformation, and thermal stability of Cu-Zr-Al bulk metallic glass, Acta Mater 212 (2021), 116923, https://doi.org/10.1016/j.actamat.2021.116923.
[9] J. Shen, Q. Chen, J. Sun, H. Fan, G. Wang, Exceptionally high glass-forming ability of an FeCoCrMoCBY alloy, Appl. Phys. Lett. 86 (15) (2005), 151907, https://doi.org/10.1063/1.1897426.
[10] N. Neuber, et al., The role of Ga addition on the thermodynamics, kinetics, and tarnishing properties of the Au-Ag-Pd-Cu-Si bulk metallic glass forming system, Acta Mater 165 (2019) 315–326, https://doi.org/10.1016/j.actamat.2018.11.052.
[11] A.J. Drehman, A.L. Greer, D. Turnbull, Bulk formation of a metallic glass: $Pd_{40}Ni_{40}P_{20}$, Appl. Phys. Lett. 41 (8) (1982) 716–717, https://doi.org/10.1063/1.93645.
[12] H.T. Hu, L.Y. Chen, X.D. Wang, Q.P. Cao, J.Z. Jiang, Formation of Ni–Nb–Zr–X (X=Ti, Ta, Fe, Cu, Co) bulk metallic glasses, J. Alloys Compd. 460 (1–2) (2008) 714–718, https://doi.org/10.1016/j.jallcom.2008.01.075.
[13] Z. Zhu, H. Zhang, D. Pan, W. Sun, Z. Hu, Fabrication of binary Ni-Nb bulk metallic glass with high strength and compressive plasticity, Adv. Eng. Mater. 8 (10) (2006) 953–957, https://doi.org/10.1002/adem.200600105.
[14] D. Li, H. Zhang, A. Wang, Z. Zhu, Z. Hu, Effect of Sn addition on the glass-forming ability and mechanical properties of Ni-Nb-Zr bulk metallic glasses, Chin. Sci. Bull. 56 (36) (2011) 3926–3931, https://doi.org/10.1007/s11434-011-4763-x.
[15] Z.W. Zhu, H.F. Zhang, B.Z. Ding, Z.Q. Hu, Synthesis and properties of bulk metallic glasses in the ternary Ni–Nb–Zr alloy system, Mater. Sci. Eng. A 492 (1–2) (2008) 221–229, https://doi.org/10.1016/j.msea.2008.04.021.
[16] H. Okamoto, Nb-Ni (Niobium–Nickel), J. Phase Equilibria Diffus. 29 (2) (2008), https://doi.org/10.1007/s11669-008-9277-0.
[17] S.M. Chathoth, B. Damaschke, M.M. Koza, K. Samwer, Dynamic singularity in multicomponent glass-forming metallic liquids, Phys. Rev. Lett. 101 (3) (2008), 037801, https://doi.org/10.1103/PhysRevLett.101.037801.
[18] L. Xia, W.H. Li, S.S. Fang, B.C. Wei, Y.D. Dong, Binary Ni–Nb bulk metallic glasses, J. Appl. Phys. 99 (2) (2006), 026103, https://doi.org/10.1063/1.2158130.
[19] D. Wang, Y. Li, B.B. Sun, M.L. Sui, K. Lu, E. Ma, Bulk metallic glass formation in the binary Cu–Zr system, Appl. Phys. Lett. 84 (20) (2004) 4029–4031, https://doi.org/10.1063/1.1751219.
[20] J.B. Qiang, et al., Binary Ni-Ta bulk metallic glasses designed by using a cluster-plus-glue-atom model, Mater. Sci. Forum 688 (2011) 395–399. 10.4028/www.scientific.net/MSF.688.395.
[21] K. Vijay Reddy, S. Pal, Contribution of Nb towards enhancement of glass forming ability and plasticity of Ni-Nb binary metallic glass, J. Non. Cryst. Solids 471 (2017) 243–250, https://doi.org/10.1016/j.jnoncrysol.2017.06.007.
[22] T.D. Xu, X.D. Wang, H. Zhang, Q.P. Cao, D.X. Zhang, J.Z. Jiang, Structural evolution and atomic dynamics in Ni–Nb metallic glasses: a molecular dynamics study, J. Chem. Phys. 147 (14) (2017), 144503, https://doi.org/10.1063/1.4995006.
[23] Y.Q. Cheng, H.W. Sheng, E. Ma, Relationship between structure, dynamics, and mechanical properties in metallic glass-forming alloys, Phys. Rev. B 78 (1) (2008), 014207, https://doi.org/10.1103/PhysRevB.78.014207.
[24] M. Shimono, H. Onodera, Dynamics and geometry of icosahedral order in liquid and glassy phases of metallic glasses, Metals (Basel). 5 (3) (2015) 1163–1187, https://doi.org/10.3390/met5031163.
[25] A. Malins, J. Eggers, C.P. Royall, S.R. Williams, H. Tanaka, Identification of long-lived clusters and their link to slow dynamics in a model glass former, J. Chem. Phys. 138 (12) (2013), https://doi.org/10.1063/1.4790515.
[26] H. Choi-Yim, D. Xu, W.L. Johnson, Ni-based bulk metallic glass formation in the Ni–Nb–Sn and Ni–Nb–Sn–X (X=B,Fe,Cu) alloy systems, Appl. Phys. Lett. 82 (7) (2003) 1030–1032, https://doi.org/10.1063/1.1544434.
[27] M. Lee, D. Bae, W. Kim, D. Kim, Ni-based refractory bulk amorphous alloys with high thermal stability, Mater. Trans. 44 (10) (2003) 2084–2087, https://doi.org/10.2320/matertrans.44.2084.
[28] T. Zhang, A. Inoue, New bulk glassy Ni-based alloys with high strength of 3000 MPa, Mater. Trans. 43 (4) (2002) 708–711, https://doi.org/10.2320/matertrans.43.708.
[29] C. Ma, H. Soejima, S. Ishihara, K. Amiya, N. Nishiyama, A. Inoue, New Ti-based bulk glassy alloys with high glass-forming ability and superior mechanical properties, Mater. Trans. 45 (11) (2004) 3223–3227, https://doi.org/10.2320/matertrans.45.3223.
[30] A. Inoue, Stabilization of supercooled liquid and opening-up of bulk glassy alloys, Proc. Japan Acad. Ser. B 73 (2) (1997) 19–24, https://doi.org/10.2183/pjab.73.19.
[31] W.H. Wang, Roles of minor additions in formation and properties of bulk metallic glasses, Prog. Mater. Sci. 52 (4) (2007) 540–596, https://doi.org/10.1016/j.pmatsci.2006.07.003.
[32] H.W. Kui, A.L. Greer, D. Turnbull, Formation of bulk metallic glass by fluxing, Appl. Phys. Lett. 45 (6) (1984) 615–616, https://doi.org/10.1063/1.95330.
[33] J. Schroers, W.L. Johnson, Highly processable bulk metallic glass-forming alloys in the Pt–Co–Ni–Cu–P system, Appl. Phys. Lett. 84 (18) (2004) 3666–3668, https://doi.org/10.1063/1.1738945.
[34] C. Suryanarayana, A. Inoue, Iron-based bulk metallic glasses, Int. Mater. Rev. 58 (3) (2013) 131–166, https://doi.org/10.1179/1743280412Y.0000000007.
[35] X. Wang, I. Yoshii, A. Inoue, Y.-.H. Kim, I.-.B. Kim, Bulk amorphous $Ni_{75-x}Nb_5M_xP_{20-y}B_y$ (M=Cr, Mo) alloys with large supercooling and high strength, Mater. Trans. JIM 40 (10) (1999) 1130–1136, https://doi.org/10.2320/matertrans1989.40.1130.

[36] A. Kawashima, H. Habazaki, K. Hashimoto, Highly corrosion-resistant Ni-based bulk amorphous alloys, Mater. Sci. Eng. A (1–2) (2001) 753–757, https://doi.org/10.1016/S0921-5093(00)01587-2.

[37] A. Kuball, et al., On the bulk glass formation in the ternary Pd-Ni-S system, Acta Mater. 158 (2018) 13–22, https://doi.org/10.1016/j.actamat.2018.07.039.

[38] N. Neuber, et al., On the thermodynamics and its connection to structure in the Pt-Pd-Cu-Ni-P bulk metallic glass forming system, Acta Mater. 220 (2021), 117300, https://doi.org/10.1016/j.actamat.2021.117300.

[39] "Amorphous Metal Solutions GmbH", 2020. https://ams-metal.de/, Date accessed: April 2023.

[40] R. Busch, B. Bochtler, O. Gross, S. Hechler, and A. Kuball, "Apparatus and method for producing a cast part formed from amorphous or partially amorphous metal, and cast part", 2020, U.S. Patent Application No. 17/253,258.

[41] D. Turnbull, Under what conditions can a glass be formed? Contemp. Phys. 10 (5) (1969) 473–488, https://doi.org/10.1080/00107516908204405.

[42] A. Kuball, et al., Development and characterization of titanium-based bulk metallic glasses, J. Alloys Compd. 790 (2019) 337–346, https://doi.org/10.1016/j.jallcom.2019.03.001.

[43] W. Rhim, et al., An electrostatic levitator for high-temperature containerless materials processing in 1-g, Rev. Sci. Instrum. 64 (10) (1993) 2961–2970, https://doi.org/10.1063/1.1144475.

[44] T. Meister, H. Werner, G. Lohoefer, D.M. Herlach, H. Unbehauen, Gain-scheduled control of an electrostatic levitator, Control Eng. Pract. 11 (2) (2003) 117–128, https://doi.org/10.1016/S0967-0661(02)00102-8.

[45] T. Kordel, et al., Neutron scattering experiments on liquid droplets using electrostatic levitation, Phys. Rev. B 83 (10) (2011), 104205, https://doi.org/10.1103/PhysRevB.83.104205.

[46] G. Ashiotis, et al., The fast azimuthal integration Python library: pyFAI, J. Appl. Crystallogr. 48 (2) (2015) 510–519, https://doi.org/10.1107/S1600576715004306.

[47] X. Qiu, J.W. Thompson, S.J.L. Billinge, PDFgetX2 : a GUI-driven program to obtain the pair distribution function from X-ray powder diffraction data, J. Appl. Crystallogr. 37 (4) (2004), https://doi.org/10.1107/S0021889804011744.

[48] Nb3Ni2P (Nb2.5Ni1.66P0.84) crystal structure: datasheet from 'PAULING FILE Multinaries edition – 2012, in: P. Villars, K. Cenzual (Eds.), Nb3Ni2P (Nb2.5Ni1.66P0.84) crystal structure: datasheet from 'PAULING FILE Multinaries edition – 2012, Springer Mater. (2022). https://materials.springer.com/isp/crystallographic/docs/sd_0540203. accessed Nov. 02.

[49] The Materials Project, "Materials data on $NbNi_3$ by materials project", 2020. https://materialsproject.org/materials/mp-1451 (accessed Oct. 28, 2022).

[50] The Materials Project, "Materials data on Nb_7Ni_6 by materials project." https://materialsproject.org/materials/mp-1104237/, (accessed Nov. 02, 2022).

[51] H. Okamoto, Ni-Ta (nickel-tantalum), J. Phase Equilibria 17 (4) (1996), https://doi.org/10.1007/BF02665571.

[52] J.H. Na, S.W. Sohn, W.T. Kim, D.H. Kim, Two-step-like anomalous glass transition behavior in Ni–Zr–Nb–Al–Ta metallic glass alloys, Scr. Mater. 57 (3) (2007) 225–228, https://doi.org/10.1016/j.scriptamat.2007.04.014.

[53] A.L. Greer, Y.Q. Cheng, E. Ma, Shear bands in metallic glasses, Mater. Sci. Eng. R Rep. 74 (4) (2013) 71–132, https://doi.org/10.1016/j.mser.2013.04.001.

[54] H.T. Angus, The significance of hardness, Wear 54 (1) (1979) 33–78, https://doi.org/10.1016/0043-1648(79)90046-2.

[55] M.K. He, S.H. Chen, P. Yu, L. Xia, Enhanced mechanical properties of $Ni_{62}Nb_{38}$ bulk metallic glasses by Ta substitution, J. Non. Cryst. Solids 471 (2017) 452–455, https://doi.org/10.1016/j.jnoncrysol.2017.07.004.

[56] A. Takeuchi, A. Inoue, Classification of bulk metallic glasses by atomic size difference, heat of mixing and period of constituent elements and its application to characterization of the main alloying element, Mater. Trans. 46 (12) (2005) 2817–2829, https://doi.org/10.2320/matertrans.46.2817.

[57] K.J. Laws, D.B. Miracle, M. Ferry, A predictive structural model for bulk metallic glasses, Nat. Commun. 6 (1) (2015) 8123, https://doi.org/10.1038/ncomms9123.

[58] Z. Lu, C. Liu, Y. Dong, Effects of atomic bonding nature and size mismatch on thermal stability and glass-forming ability of bulk metallic glasses, J. Non. Cryst. Solids 341 (1–3) (2004) 93–100, https://doi.org/10.1016/j.jnoncrysol.2004.04.024.

[59] H. Choi-Yim, R. Busch, W.L. Johnson, The effect of silicon on the glass forming ability of the $Cu_{47}Ti_{34}Zr_{11}Ni_8$ bulk metallic glass forming alloy during processing of composites, J. Appl. Phys. 83 (12) (1998) 7993–7997, https://doi.org/10.1063/1.367981.

[60] W.-.H. Wang, H.Y. Bai, Role of small atoms in the formation and properties of Zr–Ti–Cu–Ni–Be bulk amorphous alloys, J. Appl. Phys. 84 (11) (1998) 5961–5968, https://doi.org/10.1063/1.368891.

[61] A. Inoue, X... Wang, Bulk amorphous FC20 (Fe–C–Si) alloys with small amounts of B and their crystallized structure and mechanical properties, Acta Mater. 48 (6) (2000) 1383–1395, https://doi.org/10.1016/S1359-6454(99)00394-8.

[62] D.B. Miracle, The efficient cluster packing model – An atomic structural model for metallic glasses, Acta Mater. 54 (16) (2006) 4317–4336, https://doi.org/10.1016/j.actamat.2006.06.002.

[63] B. Bochtler, et al., Changes in the crystallization sequence upon sulfur addition in the $Zr_{52.5}Cu_{17.9}Ni_{14.6}Al_{10}Ti_5$ bulk metallic glass-forming liquid revealed by in situ high-energy x-ray diffraction, Phys. Rev. Mater. 5 (10) (2021), 103402, https://doi.org/10.1103/PhysRevMaterials.5.103402.

[64] A. Kuball, O. Gross, B. Bochtler, R. Busch, Sulfur-bearing metallic glasses: a new family of bulk glass-forming alloys, Scr. Mater. 146 (2018) 73–76, https://doi.org/10.1016/j.scriptamat.2017.11.011.

[65] O. Gross, L. Ruschel, A. Kuball, B. Bochtler, B. Adam, R. Busch, Bulk metallic glass formation in the (Ti,Zr)-(Ni,Cu)-S system, J. Phys. Condens. Matter 84 (20) (2020) 4029–4031, https://doi.org/10.1088/1361-648X/ab7c15.

[66] H. Wollaston, XV. On the identity of Columbium and Tantalum, Philos. Trans. R. Soc. London 99 (1809) 246–252, https://doi.org/10.1098/rstl.1809.0017.

[67] C. Ravi, B.K. Panigrahi, M.C. Valsakumar, A. van de Walle, First-principles calculation of phase equilibrium of V-Nb, V-Ta, and Nb-Ta alloys, Phys. Rev. B 85 (5) (2012), 054202, https://doi.org/10.1103/PhysRevB.85.054202.

[68] H. Men, S. Pang, A. Inoue, T. Zhang, New Ti-based bulk metallic glasses with significant plasticity, Mater. Trans. 46 (10) (2005) 2218–2220, https://doi.org/10.2320/matertrans.46.2218.

[69] P. Villars and H. Okamoto, Eds., "Nb-Ni-Ta Liquidus Projection of Ternary Phase Diagram: Datasheet from 'PAULING FILE Multinaries Edition –2012' in SpringerMaterials". Springer-Verlag Berlin Heidelberg & Material Phases Data System (MPDS), Switzerland & National Institute for Materials Science (NIMS), Japan. [Online]. Available: https://materials.springer.com/isp/phase-diagram/docs/c_1400091.

[70] L. Zhang, et al., Compressive plastic metallic glasses with exceptional glass forming ability in the Ti–Zr–Cu–Fe–Be alloy system, J. Alloys Compd. 638 (2015) 349–355, https://doi.org/10.1016/j.jallcom.2015.03.120.

[71] J. Pan, L. Liu, K.C. Chan, Enhanced plasticity by phase separation in CuZrAl bulk metallic glass with micro-addition of Fe, Scr. Mater. 60 (9) (2009) 822–825, https://doi.org/10.1016/j.scriptamat.2009.01.032.

[72] X. Wang, et al., A plastic Zr–Cu–Ag–Al bulk metallic glass, Acta Mater 59 (3) (2011) 1037–1047, https://doi.org/10.1016/j.actamat.2010.10.034.

[73] W. Lu, J.-.C. Tseng, A. Feng, J. Shen, Structural origin of the enhancement in glass-forming ability of binary Ni-Nb metallic glasses, J. Non. Cryst. Solids 564 (2021), 120834, https://doi.org/10.1016/j.jnoncrysol.2021.120834.

[74] G.R. Garrett, M.D. Demetriou, J. Chen, W.L. Johnson, Effect of microalloying on the toughness of metallic glasses, Appl. Phys. Lett. 101 (24) (2012), 241913, https://doi.org/10.1063/1.4769997.

[75] W.L. Johnson, K. Samwer, A universal criterion for plastic yielding of metallic glasses with a (T/Tg)2/3 temperature dependence, Phys. Rev. Lett. 95 (19) (2005) 2–5, https://doi.org/10.1103/PhysRevLett.95.195501.

[76] Y. Sun, A. Concustell, A.L. Greer, Thermomechanical processing of metallic glasses: extending the range of the glassy state, Nat. Rev. Mater. 1 (9) (2016) 16039, https://doi.org/10.1038/natrevmats.2016.39.